Supporting Information for "Linker-mediated Assembly of Virus-like Particles into Ordered Arrays via Electrostatic Control"

Nicholas E. Brunk,[*,†,⊥] Masaki Uchida,[*,‡,⊥] Byeongdu Lee,[*,¶] Masafumi Fukuto,[*,§,‖] Lin Yang,[*,§] Trevor Douglas,[*,‡] and Vikram Jadhao[*,†]

†*Intelligent Systems Engineering, Indiana University, Bloomington, Indiana 47408*

‡*Department of Chemistry, Indiana University, Bloomington, Indiana 47408*

¶*X-Ray Science Division, Advanced Photon Source, Argonne National Laboratory, 9700 South Cass Avenue, Illinois 60439*

§*National Synchrotron Light Source II, Brookhaven National Laboratory, Upton, New York 11973*

‖*Condensed Matter Physics and Materials Science Department, Brookhaven National Laboratory, Upton, New York 11973*

⊥*Contributed equally to this work*

E-mail: nbrunk@iu.edu; muchida@indiana.edu; blee@aps.anl.gov; fukuto@bnl.gov; lyang@bnl.gov; trevdoug@iu.edu; vjadhao@iu.edu

Experimental Details

Modulating surface charge of P22 VLPs by genetic engineering: Three variants of the P22 VLPs possessing different surface charges were prepared by genetic engineering of the C-terminus of the P22 Coat Protein (CP). Two repeats of either a net negatively charged peptide with sequence VAALEKE (E2 peptide), a neutral peptide with sequence VAALQSQ (Q2 peptide), or

net positively charged peptide with sequence VAALKEK (K2 peptide) were introduced at the C-terminus of the CP, which is exposed to the exterior of the VLP (hereafter referred to as CP-E2, CP-Q2 and CP-K2).[1] Because the P22 VLP is assembled from 420 copies of CP, up to 420 copies of the E2, Q2 or K2 peptides are displayed on the outside of the P22 VLP for each mutant. The P22 VLP variants with the E2 peptide, Q2 peptide and the K2 peptide are referred to as P22-E2, P22-Q2 and P22-K2, respectively. The DNA and amino acids sequences of CP-E2, CP-N2 and CP-K2 are shown below, after the primary SI text.

Expression and purification of P22-E2, P22-Q2, P22-K2 VLPs: The three variants of P22 VLPs were expressed and purified using an established procedure described elsewhere.[2,3] Briefly, a truncated P22 scaffolding protein (SP141) and an engineered CP were cloned into the first and the second cloning sites of the pRSFDuet-1 vector (Novagen), respectively. The vector was transformed into BL21 (DE3) E. coli strain (New England Biolabs) for protein expression. E. coli containing each vector was cultured in LB medium at 37°C in the presence of 30 μg/mL kanamycin to maintain selection pressure. Expression of the SP141 and a CP mutant was induced by isopropyl -D-thiogalactopyranoside (IPTG) to a final concentration of 0.3 mM when the OD at 600 nm of the culture medium reached 0.6 a.u. The cells were allowed to grow for an additional 4h, then harvested and stored at -80°C until the P22 VLPs were purified. The P22 VLPs self-assembled from SP141 and CP *in vivo* were purified via ultracentrifugation at 45,000 rpm over a 35% (w/v) sucrose cushion followed by size exclusion chromatography with a Sephacryl S-500 HR column (GE Healthcare Life Sciences). P22 VLPs were pelleted by ultracentrifugation and then re-suspended in phosphate buffers with various ionic strengths.

Characterization of P22 VLPs: Molecular weights of CP mutants with three different peptides were measured with ESI-Q-TOF mass spectrometry (Synapt G2S, Waters, Milford, MA) interfaced to an Acquity ultra performance liquid chromatography (UPLC; Waters) equipped with a reverse phase column (Jupiter C4 5 μm 300 Å, Phenomenex) (Fig. S2). Two microliters of the P22 sample (0.8 mg/mL) were loaded onto the column and then eluted through a gradient of

100% 0.1% formic acid in H_2O to 100% 0.1% formic acid in Acetonitrile. The deconvoluted average mass of a protein was obtained from a multiple charge state distribution and compared with a calculated molecular weight for each mutant. The overall cage-like morphology (Fig. S1) and hydrodynamic diameter (Fig. S3) of P22 VLP mutants were analyzed with transmission electron microscopy (TEM; JEM 1010 transmission electron microscope, JEOL Ltd., Akishima, Japan) and dynamic light scattering (DLS; Zetasizer Nano ZS, Malvern Instruments, Worcestershire, UK)3.

Zeta-potentials of each P22 mutant in buffer solution (sodium phosphate 10 mM, sodium chloride 20 mM, pH 7.0) were measured using Zetasizer Nano ZS (Malvern Instruments) (Fig. S4A). The Smoluchowski approximation was used to convert the electrophoretic mobility to zeta-potential. The surface charge of P22 VLPs was also qualitatively assessed using a native agarose gel. A horizontal 1% agarose gel was prepared using a Tris-acetate (TAE) buffer (Tris-base 40 mM, sodium acetate 20 mM EDTA 1 mM, pH 8.2) (Fig. S4B). The P22 VLP samples were mixed with sample buffer (25 mM sodium phosphate, 1 mM magnesium chloride, 20% sucrose, 0.02% bromophenyl blue, pH 7.4) at 1:1 (vol/vol) ratio prior to loading. The samples were subjected to electrophoresis in the TAE buffer for 3 hours at a constant voltage of 65 V. The proteins were detected after staining with Coomassie brilliant blue R-250.

Dendrimer-mediated assembly of P22 VLPs into three-dimensional arrays: Positively charged generation 6 polyamidoamine dendrimer (PAMAM G6; Sigma Aldrich, St. Louis, MO) has been shown to mediate higher order assembly of negatively VLPs.[3–5] In this study, three types of P22 VLP variants with different surface charges were mixed with PAMAM G6 under various ionic strengths. The VLP concentration in all experiments was held constant at $c_v = 37$ nM or a packing fraction of $\phi_v \approx 0.002$. The packing fraction ϕ_v was calculated as the ratio of the volume of the VLPs to the volume of the solution: $\phi_v = c_v V_v$, where c_v is the virus concentration (in nm^{-3}) and V_v is the volume of an individual virus (in nm^3). The dendrimer-mediated array formation of VLPs was first assessed by the increase in turbidity upon mixing the solutions (Fig. 1). Typically, 150 microliters of P22 VLP solution (50 nM VLP) in a phosphate buffer solution

was mixed with PAMAM G6 at a defined denderimer-VLP ratio (typically, 1000 dendrimers per VLP). The dendrimer solution was diluted with the same buffer solution at a ratio of 1:4 (vol/vol) beforehand. The increase in optical density of the VLP solutions was measured 30 min after mixing with the dendrimer solution on a UV-Vis spectrometer (Agilent 8453) at 800 nm and at room temperature. Because neither individual P22 VLPs nor dendrimer exhibit absorbance at 800 nm, observed optical density is attributed to scattering due to the formation of large particles. Four individual samples were measured at each data point yielding the average values and standard deviation. The size of the higher order assembly of VLPs in the solutions was analyzed using DLS (Fig. S6 and Fig. S22). Zeta potentials of VLP assemblies with various amount of G6 dendrimer at I = 5 mM (sodium phosphate 2.5 mM, sodium chloride 5 mM, pH 7.0) was determined by electrophoretic mobility measurements on a Malvern Zetasizer Nano ZS (Fig. S17).

Measurement of ionic strength threshold values: The ionic strength threshold indicating the onset of assembly for each VLP variant was estimated based on the change in the turbidity of the VLP solution when mixed with dendrimer solution at different ionic strengths (Fig. 1A of the main paper). Four individual samples of the same variant were measured at each I. Within the range of I values examined, there was a significant difference in the turbidity (optical density) for all P22 variants between the solution of the highest I at which P22 variant still assembled into arrays and that of the next higher ionic strength data point. For example, higher-order assembly of P22-E2 was initially examined at $I = 206, 247$, and 288 mM (besides other lower and higher ionic strengths). All four sample solutions at $I = 206$ and 247 mM showed drastic increase in optical density while solutions at $I = 288$ mM showed no significant increase. To refine the assay, higher order assembly at $I = 267$ mM was investigated as an addition, and all samples showed almost zero change in optical density. Based on this set of observations, the ionic strength threshold of P22-E2 was defined as $I_t = 247$ mM, which can be considered accurate up to the ionic strength increment of ≈ 20 mM. Estimates of uncertainty in the threshold values can be made more precise by examining the turbidity at finer ionic strength increments (e.g., measuring at multiple I values

between 247 and 267 mM for P22-E2).

The use of freshly defrosted samples (i.e., little peptide cleavage) in the current set of experiments yielded consistent results with very little effect of sample variability on the threshold values. We note that earlier studies have shown some variation in ionic threshold due to sample variability (likely due to cleavage of surface-exposed peptides over time); for example, threshold values as low as $I_t = 206$ mM have been recorded for P22-E2.[3]

Structure analysis of VLP arrays with Small-angle X-ray scattering (SAXS): The structure of the VLP arrays was interrogated with small-angle x-ray scattering (SAXS) at the X9 beamline at the National Synchrotron Light Source (NSLS) and the 12ID-B beamline at the Advanced Photon Source (APS). All the samples were subjected to the SAXS measurements in the buffer solutions as prepared. The measurements were carried out at 13.5 keV (X9) or at 14 keV (12ID-B) and the two-dimensional scattering data were collected with a Pilatus 1M detector at the X9 and a Pilatus 2M detector at the 12ID-B. Scattering angle was calibrated using silver behenate as a standard. One-dimensional SAXS profiles were acquired via averaging the two-dimensional scattering patterns. The data were represented as scattering intensity as a function of (the modulus of) scattering vector q:

$$q = \frac{4\pi}{\lambda} \sin(\theta) \tag{1}$$

where θ is half of the scattering angle and λ is the x-ray wavelength used for the measurements. Dark current frames and scattering of buffers were measured and subtracted from all data.

The overall x-ray scattering intensity $I(q)$, which is experimentally acquired by the SAXS measurement of the P22 array samples, consist of two contributions to the x-ray scattering: the form factor $P(q)$, which is inherent to the sizes and shapes of individual nanoparticles, and the structure factor $S(q)$, which is inherent to the arrangement of these nanoparticles relative to one another. The $P(q)$ of each P22 VLP mutant was obtained by measuring the SAXS profile of monodisperse P22 VLPs in a buffer solution. The $S(q)$ of the array samples was extracted from the measured $I(q)$ as described in the previous paper by using the $P(q)$.[3] Briefly, $I(q)$ is the

following combination[6] of $P(q)$ and $S(q)$:

$$I(q) = kP(q)S(q) \tag{2}$$

The constant k is a factor related to the concentration of particles. The experimentally measured small-angle x-ray scattering profile $I(q)$ of each sample is presented in Fig. S12. The comparison between measured $I(q)$, modeled $kP(q)$, and extracted $S(q)$ are presented in Fig. S13 to Fig. S19.

Estimating crystalline domain size from SAXS: Width of the x-ray diffraction peaks is a convenient parameter to assess crystallinity of samples because crystalline domain size is inversely proportional to the x-ray diffraction peak width.[6] In this study, crystalline domain size was estimated using the full width at half maximum (FWHM) of the first order diffraction peaks of each sample and the Scherrer equation as described previously[3] (Fig. S16). The first order diffraction peak was fit with Gaussian functions to determine the FWHM. Instrumental resolution Δq_{inst}, which leads to peak broadening, was taken into account and the resolution-corrected FWHM of a sample peak, Δq_{samp}, is given by the following form for a convolution of two Gaussians:

$$\Delta q_{samp} = \sqrt{\Delta q_{obs}^2 - \Delta q_{inst}^2}, \tag{3}$$

where Δq_{obs} is the FWHM of an observed diffraction peak, and Δq_{inst} for our measurement is approximately 0.0005 $\mathrm{\AA}^{-1}$. Crystalline domain size d was estimated using the Scherrer equation:

$$d = \frac{K\lambda}{\beta \cos(\theta)} \tag{4}$$

where K is Scherrer's constant, λ is the x-ray wavelength used for the measurements (0.8856 $\mathrm{\AA}$), β is the resolution-corrected peak width in radians, and θ is half of the scattering angle. Although the value of K depends on factors such as geometry of the crystallites, 0.9 may be taken for roughly equant crystallites when the FWHM is used as the measure of peak width.[7,8]

DNA sequences of proteins used in this study:

CP with E2 (CP-E2)

ATG GCT TTG AAC GAA GGT CAA ATT GTT ACA CTG GCG GTA GAT GAA ATC ATC GAA ACC ATC TCC GCA ATC ACT CCA ATG GCG CAG AAA GCC AAG AAA TAC ACC CCG CCT GCT GCT TCT ATG CAG CGC TCC AGC AAT ACC ATC TGG ATG CCT GTA GAG CAA GAG TCA CCC ACT CAG GAG GGC TGG GAT TTA ACT GAT AAA GCG ACA GGG TTA CTG GAA CTT AAC GTC GCG GTA AAC ATG GGA GAG CCG GAT AAC GAC TTC TTC CAG TTG CGT GCT GAT GAC TTG CGA GAC GAA ACT GCG TAT CGT CGC CGC ATC CAG TCT GCC GCT CGC AAG CTG GCG AAC AAC GTT GAG TTG AAA GTC GCA AAC ATG GCC GCC GAG ATG GGT TCG CTG GTT ATC ACC TCC CCT GAT GCC ATC GGC ACT AAT ACC GCA GAC GCC TGG AAC TTT GTG GCC GAC GCA GAA GAA ATC ATG TTC TCC CGC GAA CTT AAC CGC GAC ATG GGG ACA TCG TAC TTC TTC AAC CCT CAG GAC TAC AAA AAA GCG GGT TAC GAC CTG ACC AAG CGT GAC ATC TTC GGG CGT ATT CCT GAA GAA GCA TAC CGA GAT GGC ACC ATT CAG CGT CAG GTC GCT GGC TTC GAT GAT GTC CTG CGC TCT CCG AAA CTT CCT GTG CTG ACC AAA TCC ACC GCA ACT GGC ATC ACT GTA TCC GGT GCG CAG TCC TTC AAG CCT GTC GCA TGG CAA CTG GAT AAC GAT GGC AAC AAA GTT AAC GTT GAT AAC CGT TTT GCT ACC GTC ACC CTG TCT GCA ACT ACC GGC ATG AAA CGC GGC GAC AAA ATT TCG TTT GCT GGC GTT AAG TTC CTT GGT CAG ATG GCT AAG AAC GTA CTG GCT CAG GAT GCG ACT TTC TCC GTA GTC CGC GTT GTT GAC GGT ACT CAT GTT GAA ATC ACG CCG AAG CCG GTA GCG CTG GAT GAT GTT TCC CTG TCT CCG GAG CAG CGT GCC TAC GCC AAC GTT AAC ACC TCG CTG GCT GAT GCA ATG GCA GTG AAC ATT CTG AAC GTT AAA GAC GCT CGC ACT AAT GTG TTC TGG GCT GAC GAT GCT ATT CGT ATC GTG TCT CAG CCG ATT CCG GCT AAC CAT GAA CTT TTT GCA GGT ATG AAA ACT ACC TCA TTC AGC ATC CCT GAT GTT GGC CTG AAC GGT ATC TTC GCT ACG CAG GGT GAT ATT TCC ACC CTG TCC GGC CTG TGC CGT ATT GCG CTG TGG TAC GGC GTA AAC GCG ACA CGA CCG GAG GCA ATC GGT GTT GGC CTG

CCT GGT CAG ACT GCG ACT AGT GTG GCG GCG CTG GAA AAA GAA GTT GCC GCC TTG GAG AAG GAG TAG

CP with Q2 (CP-Q2)

ATG GCT TTG AAC GAA GGT CAA ATT GTT ACA CTG GCG GTA GAT GAA ATC ATC GAA ACC ATC TCC GCA ATC ACT CCA ATG GCG CAG AAA GCC AAG AAA TAC ACC CCG CCT GCT GCT TCT ATG CAG CGC TCC AGC AAT ACC ATC TGG ATG CCT GTA GAG CAA GAG TCA CCC ACT CAG GAG GGC TGG GAT TTA ACT GAT AAA GCG ACA GGG TTA CTG GAA CTT AAC GTC GCG GTA AAC ATG GGA GAG CCG GAT AAC GAC TTC TTC CAG TTG CGT GCT GAT GAC TTG CGA GAC GAA ACT GCG TAT CGT CGC CGC ATC CAG TCT GCC GCT CGC AAG CTG GCG AAC AAC GTT GAG TTG AAA GTC GCA AAC ATG GCC GCC GAG ATG GGT TCG CTG GTT ATC ACC TCC CCT GAT GCC ATC GGC ACT AAT ACC GCA GAC GCC TGG AAC TTT GTG GCC GAC GCA GAA GAA ATC ATG TTC TCC CGC GAA CTT AAC CGC GAC ATG GGG ACA TCG TAC TTC TTC AAC CCT CAG GAC TAC AAA AAA GCG GGT TAC GAC CTG ACC AAG CGT GAC ATC TTC GGG CGT ATT CCT GAA GAA GCA TAC CGA GAT GGC ACC ATT CAG CGT CAG GTC GCT GGC TTC GAT GAT GTC CTG CGC TCT CCG AAA CTT CCT GTG CTG ACC AAA TCC ACC GCA ACT GGC ATC ACT GTA TCC GGT GCG CAG TCC TTC AAG CCT GTC GCA TGG CAA CTG GAT AAC GAT GGC AAC AAA GTT AAC GTT GAT AAC CGT TTT GCT ACC GTC ACC CTG TCT GCA ACT ACC GGC ATG AAA CGC GGC GAC AAA ATT TCG TTT GCT GGC GTT AAG TTC CTT GGT CAG ATG GCT AAG AAC GTA CTG GCT CAG GAT GCG ACT TTC TCC GTA GTC CGC GTT GTT GAC GGT ACT CAT GTT GAA ATC ACG CCG AAG CCG GTA GCG CTG GAT GAT GTT TCC CTG TCT CCG GAG CAG CGT GCC TAC GCC AAC GTT AAC ACC TCG CTG GCT GAT GCA ATG GCA GTG AAC ATT CTG AAC GTT AAA GAC GCT CGC ACT AAT GTG TTC TGG GCT GAC GAT GCT ATT CGT ATC GTG TCT CAG CCG ATT CCG GCT AAC CAT GAA CTT TTT GCA GGT ATG AAA ACT ACC TCA TTC AGC ATC CCT GAT GTT GGC CTG AAC GGT ATC TTC GCT ACG CAG GGT GAT ATT TCC ACC CTG TCC GGC CTG TGC CGT ATT GCG

CTG TGG TAC GGC GTA AAC GCG ACA CGA CCG GAG GCA ATC GGT GTT GGC CTG CCT GGT CAG ACT GCG ACT AGT GTG GCG GCG CTG CAG AGC CAA GTG GCG GCG CTT CAA AGT CAG TAA

CP with K2 (CP-K2)

ATG GCT TTG AAC GAA GGT CAA ATT GTT ACA CTG GCG GTA GAT GAA ATC ATC GAA ACC ATC TCC GCA ATC ACT CCA ATG GCG CAG AAA GCC AAG AAA TAC ACC CCG CCT GCT GCT TCT ATG CAG CGC TCC AGC AAT ACC ATC TGG ATG CCT GTA GAG CAA GAG TCA CCC ACT CAG GAG GGC TGG GAT TTA ACT GAT AAA GCG ACA GGG TTA CTG GAA CTT AAC GTC GCG GTA AAC ATG GGA GAG CCG GAT AAC GAC TTC TTC CAG TTG CGT GCT GAT GAC TTG CGA GAC GAA ACT GCG TAT CGT CGC CGC ATC CAG TCT GCC GCT CGC AAG CTG GCG AAC AAC GTT GAG TTG AAA GTC GCA AAC ATG GCC GCC GAG ATG GGT TCG CTG GTT ATC ACC TCC CCT GAT GCC ATC GGC ACT AAT ACC GCA GAC GCC TGG AAC TTT GTG GCC GAC GCA GAA GAA ATC ATG TTC TCC CGC GAA CTT AAC CGC GAC ATG GGG ACA TCG TAC TTC TTC AAC CCT CAG GAC TAC AAA AAA GCG GGT TAC GAC CTG ACC AAG CGT GAC ATC TTC GGG CGT ATT CCT GAA GAA GCA TAC CGA GAT GGC ACC ATT CAG CGT CAG GTC GCT GGC TTC GAT GAT GTC CTG CGC TCT CCG AAA CTT CCT GTG CTG ACC AAA TCC ACC GCA ACT GGC ATC ACT GTA TCC GGT GCG CAG TCC TTC AAG CCT GTC GCA TGG CAA CTG GAT AAC GAT GGC AAC AAA GTT AAC GTT GAT AAC CGT TTT GCT ACC GTC ACC CTG TCT GCA ACT ACC GGC ATG AAA CGC GGC GAC AAA ATT TCG TTT GCT GGC GTT AAG TTC CTT GGT CAG ATG GCT AAG AAC GTA CTG GCT CAG GAT GCG ACT TTC TCC GTA GTC CGC GTT GTT GAC GGT ACT CAT GTT GAA ATC ACG CCG AAG CCG GTA GCG CTG GAT GAT GTT TCC CTG TCT CCG GAG CAG CGT GCC TAC GCC AAC GTT AAC ACC TCG CTG GCT GAT GCA ATG GCA GTG AAC ATT CTG AAC GTT AAA GAC GCT CGC ACT AAT GTG TTC TGG GCT GAC GAT GCT ATT CGT ATC GTG TCT CAG CCG ATT CCG GCT AAC CAT GAA CTT TTT GCA GGT ATG AAA ACT ACC TCA TTC AGC ATC CCT GAT GTT GGC CTG AAC GGT ATC

TTC GCT ACG CAG GGT GAT ATT TCC ACC CTG TCC GGC CTG TGC CGT ATT GCG CTG TGG TAC GGC GTA AAC GCG ACA CGA CCG GAG GCA ATC GGT GTT GGC CTG CCT GGT CAG ACT GCG ACT AGG GTG GCG GCG CTG AAA GAA AAA GTT GCC GCC TTA AAG GAG AAG TAG

SP141

ATG GGC AGC AGC CAT CAC CAT CAT CAC CAC AGC CAG GAT CCC TGG TGC CGC GCG GCA GCA TGT CGC AGC AAT GCC GTA GCA GAA CAG GGC CGC AAG ACT CAG GAG TTT ACC CAG CAA TCA GCG CAA TAC GTC GAA GCT GCC CGC AAA CAC TAT GAC GCG GCG GAA AAG CTC AAC ATC CCT GAC TAT CAG GAG AAA GAA GAC GCA TTT ATG CAA CTG GTT CCG CCT GCG GTT GGG GCC GAC ATT ATG CGC CTG TTC CCG GAA AAG TCC GCC GCG CTC ATG TAT CAC CTG GGG GCA AAC CCG GAG AAA GCC CGC CAG TTA CTG GCG ATG GAT GGG CAG TCC GCG CTG ATT GAA CTC ACT CGA CTA TCC GAA CGC TTA ACT CTC AAG CCT CGC GGT AAA CAA ATC TCT TCC GCT CCC CAT GCT GAC CAG CCT ATT ACC GGT GAT GTC AGC GCA GCA AAT AAA GAT GCC ATT CGT AAA CAA ATG GAT GCT GCT GCG AGC AAG GGA GAT GTG GAA ACC TAC CGC AAG CTA AAG GCA AAA CTT AAA GGA ATC CGA TAA

Amino acid sequences of proteins used in this study:

Note: The bold part in CP-E2, CP-Q2, and CP-K2 sequences corresponds to E2, Q2, and K2 peptides respectively.

CP-E2

MALNEGQIVTLAVDEIIETISAITPMAQKAKKYTPPAASMQRSSNTIWMPVEQESPTQEG WDLTDKATGLLELNVAVNMGEPDNDFFQLRADDLRDETAYRRRIQSAARKLANNVEL KVANMAAEMGSLVITSPDAIGTNTADAWNFVADAEEIMFSRELNRDMGTSYFFNPQDY KKAGYDLTKRDIFGRIPEEAYRDGTIQRQVAGFDDVLRSPKLPVLTKSTATGITVSGAQS FKPVAWQLDNDGNKVNVDNRFATVTLSATTGMKRGDKISFAGVKFLGQMAKNVLAQ DATFSVVRVVDGTHVEITPKPVALDDVSLSPEQRAYANVNTSLADAMAVNILNVKDAR

TNVFWADDAIRIVSQPIPANHELFAGMKTTSFSIPDVGLNGIFATQGDISTLSGLCRIALW

YGVNATRPEAIGVGLPGQTATS**VAALEKEVAALEKE**

CP-Q2

MALNEGQIVTLAVDEIIETISAITPMAQKAKKYTPPAASMQRSSNTIWMPVEQESPTQEG

WDLTDKATGLLELNVAVNMGEPDNDFFQLRADDLRDETAYRRRIQSAARKLANNVEL

KVANMAAEMGSLVITSPDAIGTNTADAWNFVADAEEIMFSRELNRDMGTSYFFNPQDY

KKAGYDLTKRDIFGRIPEEAYRDGTIQRQVAGFDDVLRSPKLPVLTKSTATGITVSGAQS

FKPVAWQLDNDGNKVNVDNRFATVTLSATTGMKRGDKISFAGVKFLGQMAKNVLAQ

DATFSVVRVVDGTHVEITPKPVALDDVSLSPEQRAYANVNTSLADAMAVNILNVKDAR

TNVFWADDAIRIVSQPIPANHELFAGMKTTSFSIPDVGLNGIFATQGDISTLSGLCRIALW

YGVNATRPEAIGVGLPGQTATS**VAALQSQVAALQSQ**

CP-K2

MALNEGQIVTLAVDEIIETISAITPMAQKAKKYTPPAASMQRSSNTIWMPVEQESPTQEG

WDLTDKATGLLELNVAVNMGEPDNDFFQLRADDLRDETAYRRRIQSAARKLANNVEL

KVANMAAEMGSLVITSPDAIGTNTADAWNFVADAEEIMFSRELNRDMGTSYFFNPQDY

KKAGYDLTKRDIFGRIPEEAYRDGTIQRQVAGFDDVLRSPKLPVLTKSTATGITVSGAQS

FKPVAWQLDNDGNKVNVDNRFATVTLSATTGMKRGDKISFAGVKFLGQMAKNVLAQ

DATFSVVRVVDGTHVEITPKPVALDDVSLSPEQRAYANVNTSLADAMAVNILNVKDAR

TNVFWADDAIRIVSQPIPANHELFAGMKTTSFSIPDVGLNGIFATQGDISTLSGLCRIALW

YGVNATRPEAIGVGLPGQTATR**VAALKEKVAALKEK**

SP141

MGSSHHHHHHSQDPWCRAAACRSNAVAEQGRKTQEFTQQSAQYVEAARKHYDAAEK

LNIPDYQEKEDAFMQLVPPAVGADIMRLFPEKSAALMYHLGANPEKARQLLAMDGQSA

LIELTRLSERLTLKPRGKQISSAPHADQPITGDVSAANKDAIRKQMDAAASKGDVETYRK

LKAKLKGIR

Model and Simulation Details

Coarse-graining solvent and ions: The solvent (water) was treated as a continuous medium in the coarse-grained model and its effect was incorporated implicitly by scaling the electrostatic forces on virus-like particles (VLPs) and dendrimers by the relative dielectric permittivity of water ($\epsilon_w = 78.54$). All hydrodynamic interactions were neglected. Similarly, to speed-up the simulations, the effects of the salt ions (NaCl, Sodium Phosphate) were modeled implicitly by introducing the screened Yukawa potential (equation 1 of the main text) characterized by a surface charge parameter q and the Debye length κ^{-1} (that varied between 0.5 and 3 nm over the range of ionic strengths studied). While using a single adjustable parameter q to describe the charged VLP and dendrimer surface enables an effective minimal model representation of the larger-scale VLP assembly phenomena, it is not expected to comprehensively capture the role of neglected effects at the coarse-grained level.[9] These effects include excluded volume effects due to finite ion sizes, electrostatic correlations between ions, and inhomogeneities in the surface charge distribution. Appropriate q values for VLP assembly studies were selected using a combination of experimentally-informed analytical approximations and simulation data-driven approach (see below).

Modeling steric effects: P22 VLPs and G6 PAMAM dendrimers were modeled as rigid spheres interacting sterically via a modified repulsive Lennard-Jones (LJ) potential (equation 2 of the main text). van der Waals attractive forces between particles were neglected as they are much weaker compared to the inter-particle electrostatic attraction at the probed length scales. The addition of peptides on the bare VLP surface is expected to modulate the accessibility and proximity of the dendrimers to the VLP surface. Dendrimers are also relatively deformable and are expected to conform to the VLP surface,[10] which can further alter their steric interaction with the VLPs. These effects were incorporated in the coarse-grained steric potential via the parameter σ_{hc}. σ_{hc} was chosen to be 6.7 nm for all the three VLP variants. This value allows for a VLP-dendrimer closest approach distance of ≈ 30.7 nm, which is ≈ 0.6 nm smaller than the VLP-dendrimer touch-

ing distance, in agreement with previously reported SAXS-based experimental assessments of the nearest neighbor spacing between two P22-E2 VLPs in an ordered array bridged by an interstitial dendrimer[3] (shown to be approximately 61.5 nm). We note that for the chosen $\sigma_{\text{hc}} = 6.7$ nm, the dendrimer-dendrimer steric repulsion reduced to the standard LJ potential (as dendrimer diameter $\sigma_d = 6.7$ nm).

Simulations show the number of condensed dendrimers to be critical to both the order acquired and assembly itself. If under-condensation occurs, assembly is severely diminished; if there is over-condensation, assembly into amorphous aggregates occurs. The equilibrium number of condensed dendrimers per VLP depends on the net VLP-dendrimer interaction. Decreasing σ_{hc} increases the steric repulsion, modulating the VLP-dendrimer potential and thus the number of condensed dendrimers at a given ionic strength. A plot of the net VLP-dendrimer interaction potential (including electrostatic interaction) with curves corresponding to different values of σ_{hc} is shown in Fig. S5. Changing σ_{hc} tunes the value of the potential minimum and the average distance of closest approach.

Modeling electrostatic interactions: VLPs were modeled as uniformly charged spheres of radius $a = 28$ nm that electrostatically interact with other VLPs and dendrimers via a screened Yukawa potential (Equation 1 of the main text) characterized by a surface charge parameter q_v and the Debye length κ^{-1}. P22-E2, P22-Q2, and P22-K2 exhibited a ζ potential of -30.4 mV, -23.6 mV, and -12.8 mV at 41.1 mM, pH = 7 respectively. Given these experimental measurements were performed close to the lowest ionic strength I, ζ for higher I values is expected to be further reduced. As $a \gg \kappa^{-1}$ and ζ values are small ($\lesssim 1.2k_BT/e$) over a wide range of I values, an approximate estimate for the net surface charge parameter q_v was obtained using the relation $q_v = \tilde{a}(1+\kappa\tilde{a})\zeta/l_B$.[11] Here $\tilde{a}$ is the radius of the VLP out to the shear surface associated with the ζ potential measurement, often approximated as $\tilde{a} = a + \kappa^{-1}$ (note $a \gg \kappa^{-1}$). The linear correlation between q_v and ζ, as outlined in this equation, was assumed; accordingly, q_v for P22-Q2 and P22-K2 were chosen to be approximately 4/5 and 2/5 of the q_v value for P22-E2.

To estimate q_v for P22-E2, a number of factors were considered. First, an upper bound on the value of q_v was established to be $\bar{q}_v \approx -3300e$ from sequence analysis assuming all residues are charged.[12] Next, q_v was correlated with ζ measurements of P22-E2 for multiple values of I to estimate plausible values for surface charge $\tilde{q}_v$ following $\tilde{q}_v = \tilde{a}(1 + \kappa\tilde{a})\zeta/l_B$. Both $\zeta = -30.4$ mV at 41.1 mM and $\zeta = -13.5$ mV at 206 mM yielded $\tilde{q}_v \approx -1000e$. Utilizing $\bar{q}_v$ and $\tilde{q}_v$ as input, a sweep of q_v values between $-500e$ and $-3300e$ was performed (for different dendrimer surface charge parameters; see below), and the P22-E2 VLP assembly for a range of I was monitored. $q_v \approx -1500e$ produced the best alignment with experimental data near ionic strength threshold for the bulk assembly of P22-E2. Using $q_v = -1500e$ for P22-E2 and the aforementioned linear correlation between q_v and ζ, q_v values for P22-Q2 and P22-K2 VLPs were chosen to be $-1200e$ and $-600e$ respectively.

G6 PAMAM dendrimers were modeled as uniformly charged spheres of radius $a_d = 3.35$ nm and effective surface charge q_d. Unlike VLPs, dendrimers exhibit a dendritic topology and are small ($a_d \sim \kappa^{-1}$), making estimation of q_d more challenging and ambiguous. It is expected that a significant fraction of the 256 terminal amine groups of a G6 PAMAM dendrimer will be dissociated at pH = 7.[13,14] However, strong counterion condensation is expected to occur in such charged dendrimer systems, leading to significant charge renormalization effects.[13,15] Experimental and analytical studies produce an estimate for G6 PAMAM dendrimers at $I = 1$ mM of $q_d \approx 15e$ in experiments, and $q_d \approx 35e$ from theoretical arguments;[13] these are also similar to those obtained for a different type of dendrimer with a comparable excess of terminal amines.[15] With these inputs in mind, a sweep over q_d between $20e$ and $45e$ was performed and the P22-E2 VLP assembly was monitored as a function of I ranging from 10 mM to 350 mM. The assembly characteristics were found to be in highest alignment with experiments for $q_v \approx -1500e, q_d \approx 35e$. Thus, for all VLP assembly studies, q_d was chosen to be $35e$. Again, charge renormalization effects as a function of ionic strength were neglected given surface roughness and other considerations limiting the capacity to theoretically estimate this variability.

A sweep over a larger q_v range yielded more VLP, dendrimer combinations that replicated the

experimentally observed P22-E2 assembly trends (e.g, $q_v \approx -2600e, q_d \approx 20e$) indicating that some ambiguity and variability exists in selecting effective charge parameters to describe coarse-grained VLP and dendrimer surfaces. These different combinations produced similar net VLP-dendrimer interaction potential (including steric interaction) of $-5\,k_BT$ at the distance of closest approach for the ionic strength threshold corresponding to the bulk assembly of P22-E2, making this potential a key feature of the minimal model representation.

Simulation details: Starting from a random configuration, all simulations were performed in an NVT ensemble within a cubic, periodic simulation box. A Nose-Hoover thermostat was employed to keep the temperature fixed at $T = 298$ K. The thermostat timescale (damping parameter) was $\tau_t = 100\Delta t$, where $\Delta t \approx 4$ ps denotes the simulation timestep. At periodic intervals during the simulation, the position coordinates of the dendrimers and VLPs were stored for post-processing to compute structural quantities such as the pair correlation functions, VLP-bound dendrimer fractions, as well as kinetic information. The majority of simulations reported used 108 VLPs and 108,000 dendrimers. Additional simulations with $\approx 5\times$ more number of particles were performed to examine finite size effects at the ionic strength thresholds for each VLP variant. Simulations were implemented in the Large-scale Atomic/Molecular Massively Parallel Simulator software (LAMMPS, 31Mar17 build)[16] on Indiana University's Big Red II supercomputer. A typical simulation took approximately 200 hours to complete using MPI acceleration between 32 Cray XE6 nodes.

Post-processing: Post-processing was done using a combination of code written in C++ and Wolfram Research's Mathematica 11.2.[17] The radius of gyration was computed in Mathematica 11.2 by first 'crawling' through all VLPs to identify the largest cluster (a contingent subset within $1.25\sigma_v$ of one another), then accounting for periodicity in all directions and computing the following:

$$R_g = \sqrt{\frac{1}{N}\sum_{k=1}^{N}(r_k - \bar{r})^2}, \tag{5}$$

where N is the total number of VLPs in the cluster, r_k is the position vector of the k^{th} VLP, and $\bar{r}$ is the mean position of all VLPs in the cluster.

VLP-VLP pair correlation functions were computed taking account of periodicity of the box and were found to be convergent using a bin width of $\delta r = 0.005\sigma_v = 0.28$ nm, where σ_v is the VLP diameter. To assess the number of VLP-bound dendrimers, a nearest neighbor algorithm with fixed-distance cutoff was used with the fixed distance of $1.05(\sigma_v + \sigma_d)/2$, that is equal to five percent beyond the touching distance of the particles.[18]

References

(1) Servid, A.; Jordan, P.; ONeil, A.; Prevelige, P.; Douglas, T. Location of the bacteriophage P22 coat protein C-terminus provides opportunities for the design of capsid-based materials. *Biomacromolecules* **2013**, *14*, 2989–2995.

(2) Kang, S.; Uchida, M.; ONeil, A.; Li, R.; Prevelige, P. E.; Douglas, T. Implementation of p22 viral capsids as nanoplatforms. *Biomacromolecules* **2010**, *11*, 2804–2809.

(3) Uchida, M.; McCoy, K.; Fukuto, M.; Yang, L.; Yoshimura, H.; Miettinen, H. M.; LaFrance, B.; Patterson, D. P.; Schwarz, B.; Karty, J. A.; Prevelige, P. E.; Lee, B.; Douglas, T. Modular Self-Assembly of Protein Cage Lattices for Multistep Catalysis. *ACS Nano* **2018**, *12*, 942–953, DOI: 10.1021/acsnano.7b06049, PMID: 29131580.

(4) Kostiainen, M. A.; Hiekkataipale, P.; Laiho, A.; Lemieux, V.; Seitsonen, J.; Ruokolainen, J.; Ceci, P. Electrostatic assembly of binary nanoparticle superlattices using protein cages. *Nature nanotechnology* **2013**, *8*, 52.

(5) McCoy, K.; Uchida, M.; Lee, B.; Douglas, T. Templated Assembly of a Functional Ordered Protein Macromolecular Framework from P22 Virus-like Particles. *ACS nano* **2018**, *12*, 3541–3550.

(6) Li, T.; Senesi, A. J.; Lee, B. Small angle X-ray scattering for nanoparticle research. *Chemical reviews* **2016**, *116*, 11128–11180.

(7) Hummer, D. R.; Heaney, P. J.; Post, J. E. In situ observations of particle size evolution during the hydrothermal crystallization of TiO2: a time-resolved synchrotron SAXS and WAXS study. *Journal of Crystal Growth* **2012**, *344*, 51–58.

(8) Langford, J. I.; Wilson, A. Scherrer after sixty years: a survey and some new results in the determination of crystallite size. *Journal of Applied Crystallography* **1978**, *11*, 102–113.

(9) Hartkamp, R.; Biance, A.-L.; Fu, L.; Dufrêche, J.-F.; Bonhomme, O.; Joly, L. Measuring surface charge: why experimental characterization and molecular modeling should be coupled. *Current Opinion in Colloid & Interface Science* **2018**,

(10) Li, J.; Piehler, L.; Qin, D.; Baker, J.; Tomalia, D.; Meier, D. Visualization and characterization of poly (amidoamine) dendrimers by atomic force microscopy. *Langmuir* **2000**, *16*, 5613–5616.

(11) Hunter, R. J. *Zeta potential in colloid science: principles and applications*; Academic press, 2013; Vol. 2.

(12) Božič, A. L.; Šiber, A.; Podgornik, R. How simple can a model of an empty viral capsid be? Charge distributions in viral capsids. *Journal of biological physics* **2012**, *38*, 657–671.

(13) Pericet-Camara, R.; Papastavrou, G.; Borkovec, M. Effective charge of adsorbed poly (amidoamine) dendrimers from direct force measurements. *Macromolecules* **2009**, *42*, 1749–1758.

(14) Maiti, P. K.; Messina, R. Counterion distribution and ζ-potential in PAMAM dendrimer. *Macromolecules* **2008**, *41*, 5002–5006.

(15) Xu, X.; Ran, Q.; Haag, R.; Ballauff, M.; Dzubiella, J. Charged dendrimers revisited: Effective charge and surface potential of dendritic polyglycerol sulfate. *Macromolecules* **2017**, *50*, 4759–4769.

(16) Plimpton, S. Fast Parallel Algorithms for Short-Range Molecular Dynamics. *Journal of Computational Physics* **1995**, *117*, 1–19, DOI: https://doi.org/10.1006/jcph.1995.1039.

(17) Wolfram Research Inc., Mathematica, Version 11.2. 2017; Champaign, IL.

(18) van Meel, J. A.; Filion, L.; Valeriani, C.; Frenkel, D. A parameter-free, solid-angle based, nearest-neighbor algorithm. *The Journal of chemical physics* **2012**, *136*, 234107.

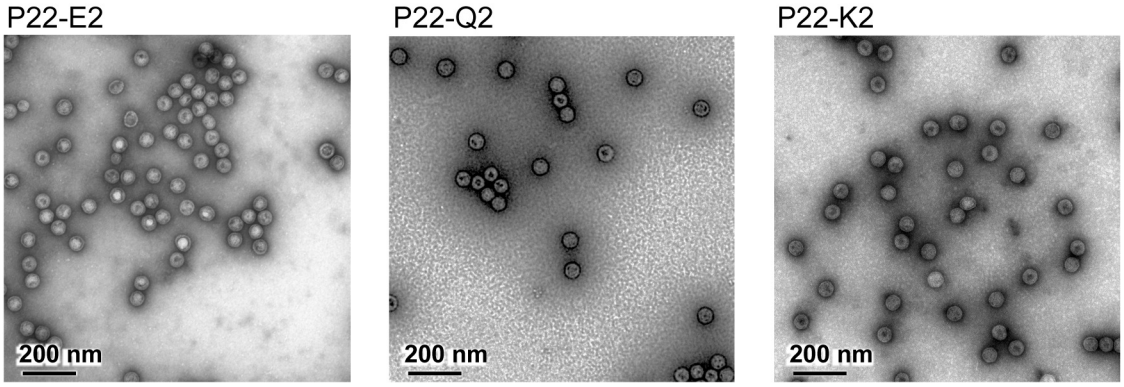

Figure S1: TEM images of P22-E2, P22-Q2 and P22-K2 VLPs. All the VLP constructs assembled into capsid structures with diameters of about 55 nm regardless of the modifications to the coat proteins (CPs), indicating that the genetic fusion of the extra peptide (i.e. (VAALEKE)2, (VAALQSQ)2, or (VAALKEK)2)) at the C-terminus of the CP did not interfere with the self-assembly of the CP subunits into the VLP capsids. The samples were stained with 2% uranyl acetate.

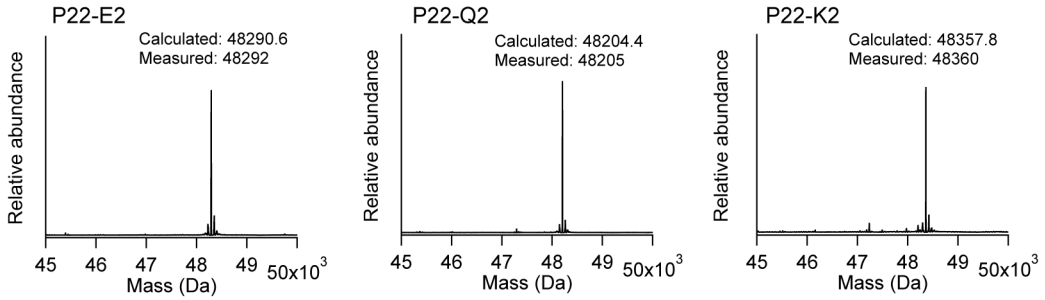

Figure S2: Deconvoluted mass analyses of CP (coat protein) mutants fused with E2 (left), Q2 (center), or K2 (right) mutants. The observed molecular weight of all three mutants are similar and agreed well with the calculated mass of each CP. Each P22 variant is composed of 420 copies of a CP mutant subunit.

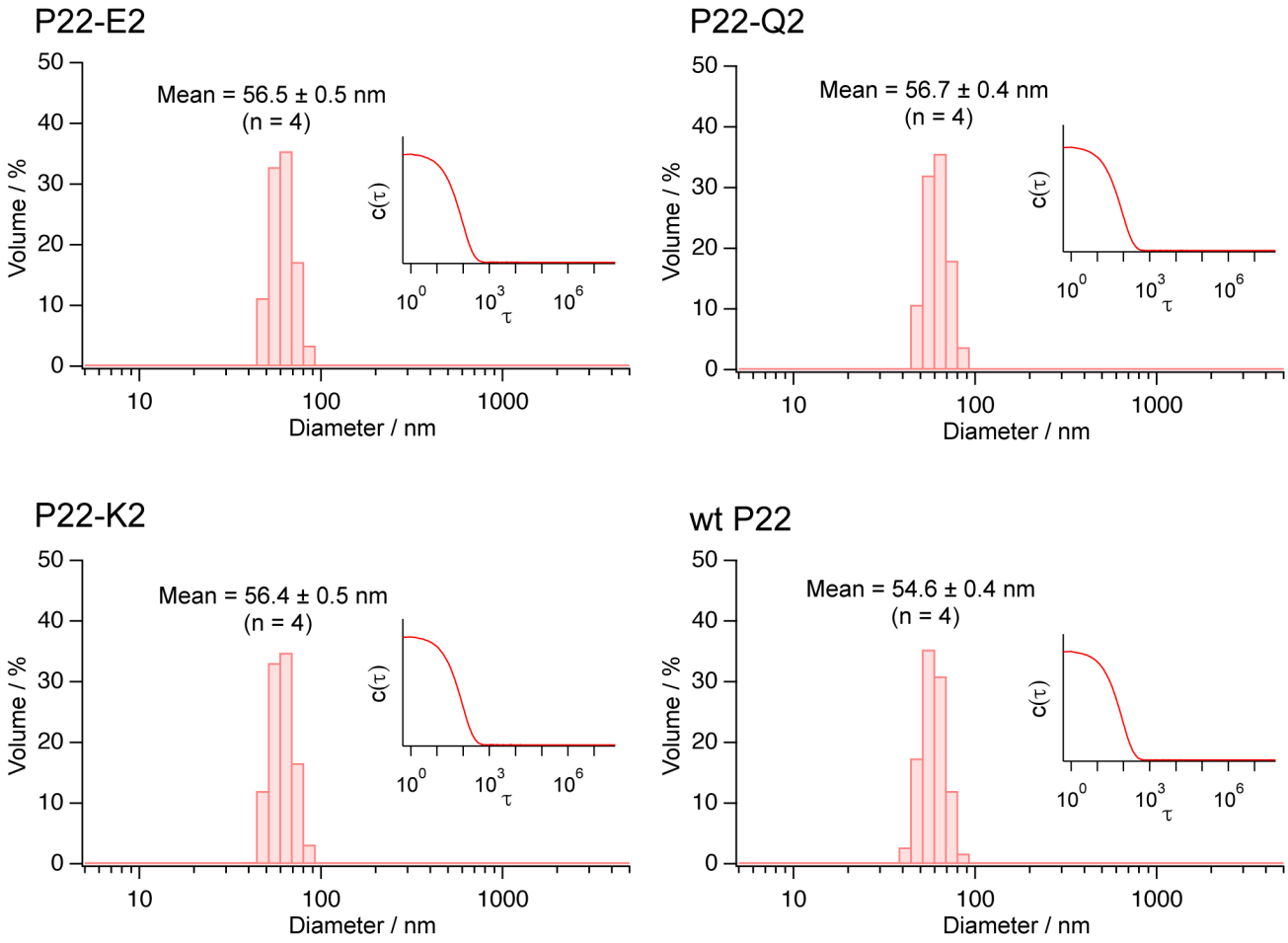

Figure S3: Volume-averaged hydrodynamic diameter of P22-E2, P22-Q2, P22-K2 and wtP22 VLPs measured with DLS and corresponding correlation functions (inset). Hydrodynamic diameters of P22-E2, P22-Q2 and P22-K2 were nearly identical to each other and about 2 nm larger than that of wtP22. Because up to 420 copies of E2, Q2 and K2 peptide could be presented on the exterior surface of the P22-E2, P22-Q2 and P22-K2 VLPs, respectively, it is reasonable to expect these mutants to have slightly larger diameter compared to wtP22 VLP. The mean and standard deviation for each variant was obtained from four repeated measurements. The size distribution histograms and corresponding correlation functions shown here are representative of the four measurements. The measurements were conducted at 25°C.

a

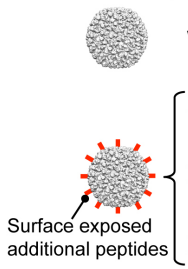

	Additional peptide	Hydrodynamic diameter /nm	Zeta potential / mV	Threshold ionic strength (I_T) / mM
wtP22	-	54.6 ± 0.4	-30.7 ± 2.3	247
P22-E2	$(VAALEKE)_2$	56.5 ± 0.5	-30.4 ± 2.8	247
P22-Q2	$(VAALQSQ)_2$	56.7 ± 0.4	-23.6 ± 2.0	123
P22-K2	$(VAALKEK)_2$	56.4 ± 0.5	-12.8 ± 2.1	61.7

b

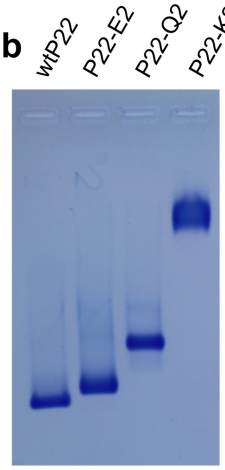

Figure S4: Summary of P22 VLP variants and assessment of their surface charges. (a) Table showing the peptide added to the C-terminus of each P22 variant (second column), the resulting hydrodynamic diameter (third column), zeta potential at pH 7.0 and ionic strength of 41.1 mM ($n = 4$ measurements); the final column shows the threshold ionic strength I_t above which the dendrimer-mediated assembly of VLPs into ordered arrays was not observed. Wild type P22 showed a negative surface charge of -30.7 mV. P22-Q2 exhibited a less negative surface charge than wtP22 and P22-K2 exhibited the least negative surface charge. P22-E2 showed a negative surface charge almost identical to wtP22, suggesting that the negatively charged E2 peptide does not alter the overall surface charge of the VLP. The zeta potential estimates were taken at $15°$C. (b) Native agarose gel electrophoresis of wtP22, P22-E2, P22-Q2 and P22-K2 VLPs. All samples moved toward the anode, which indicates net negative surface charge. Because the molecular weight and hydrodynamic diameter of P22-E2, P22-Q2 and P22-K2 are almost identical (Fig. S2 and Fig. S3), the mobility largely depends on their surface charge, indicating that P22-E2 and P22-K2 are the most and least negatively charged, respectively. The migration distance of wtP22 was slightly larger than that of P22-E2 despite the zeta potential of the two samples being nearly identical. This is likely due to the smaller size of wtP22 compared to P22-E2.

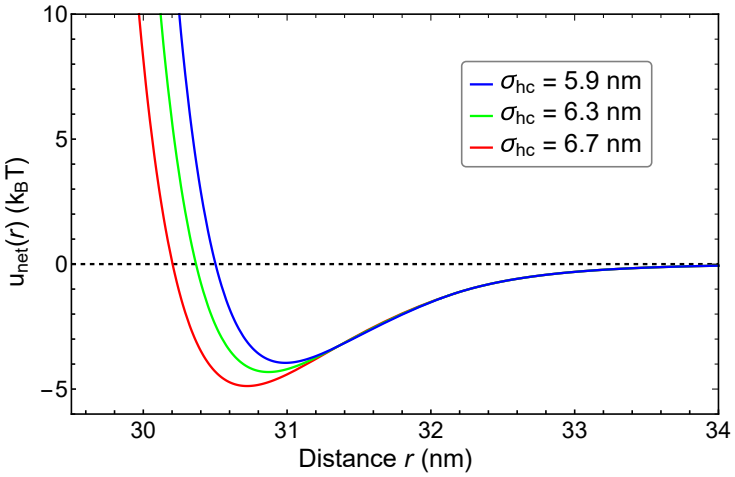

Figure S5: Net VLP-dendrimer potential, $u_{\text{net}}(r) = u_{\text{LJ}}(r) + u_{\text{E}}(r)$, for different values of σ_{hc} at the ionic strength threshold of 225 mM for the P22-E2 VLP system. Decreasing σ_{hc} increases steric repulsion and thus decreases the extent to which the dendrimer may approach the VLP. It can be seen that the distance of closest approach at which the energy minimum occurs rises as σ_{hc} is decreased, with the red curve calibrated using experimental nearest-neighbor distance between two P22-E2 VLPs bridged by a dendrimer in an ordered array.

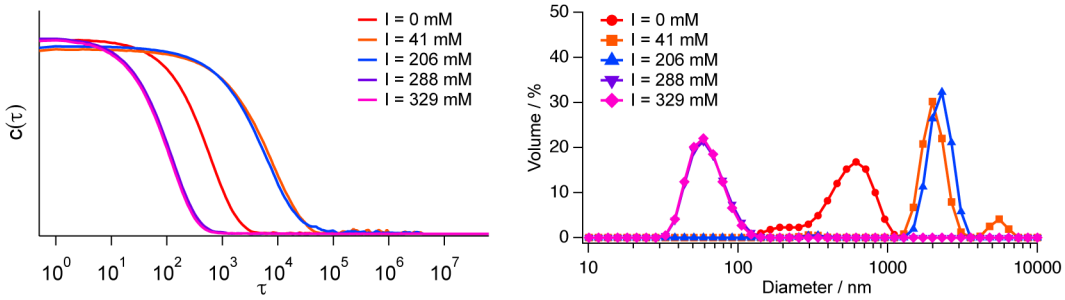

Figure S6: Correlation functions (left) and corresponding volume-averaged hydrodynamic diameter distributions (right) from DLS measurements of P22-E2 assembly when P22-E2 VLPs were mixed with 1000 PAMAM G6 dendrimers per VLP at different solution ionic strength I. For I between 41 and 247 mM, large assemblies of VLPs with aggregate diameter of a few micrometers were formed. For $I = 0$ mM solution, P22-E2 VLPs assembled into arrays but the size was significantly smaller. Above the threshold ionic strength (247 mM), the measured size was around 60 nm, indicating that P22-E2 VLPs were mono-dispersed in the solution and did not form large aggregates.

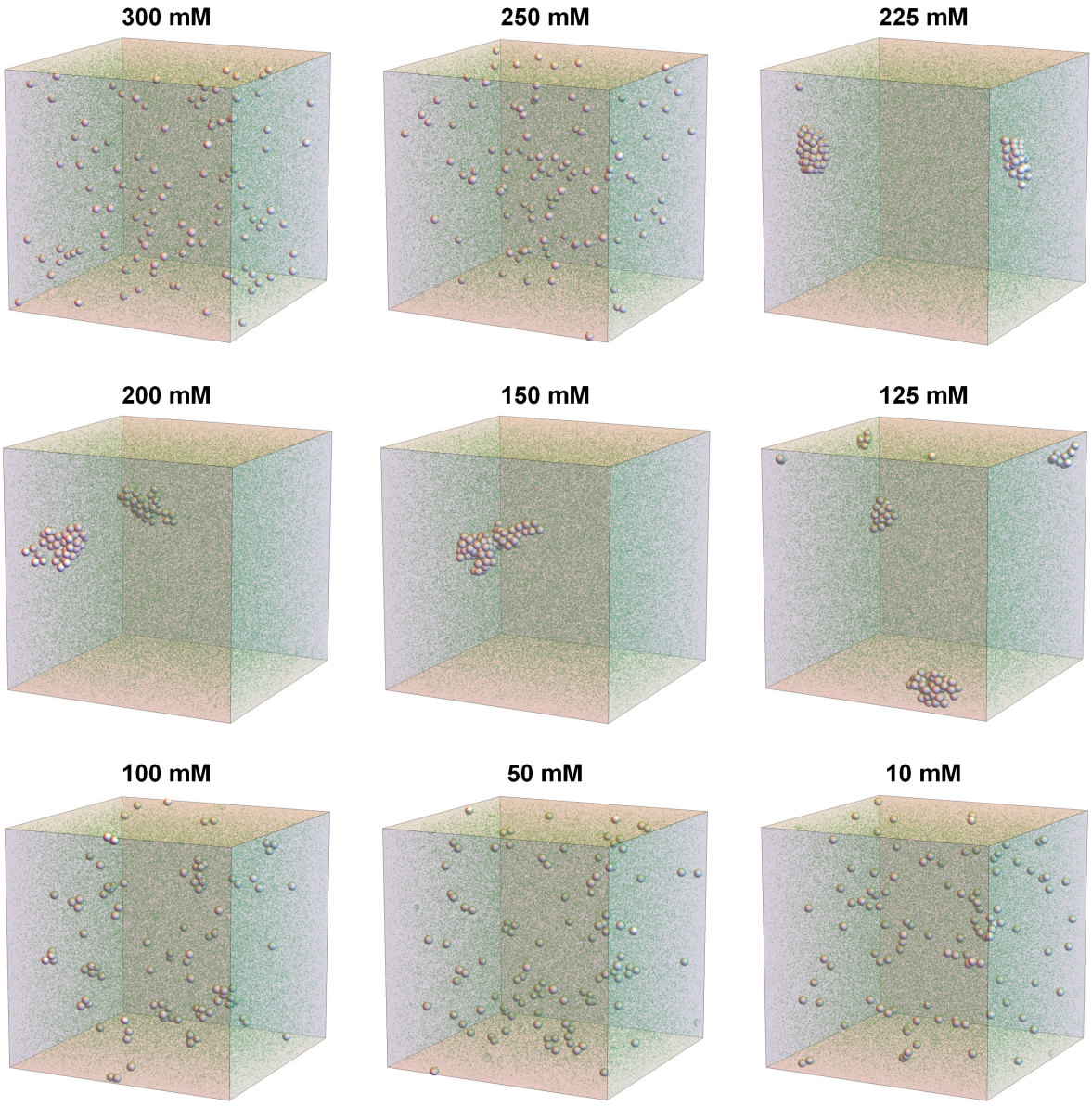

Figure S7: Representative snapshots of typical steady-state configurations of the P22-E2 system; silver spheres are VLPs and smaller green spheres are dendrimers. Ionic strength I decreases from top to bottom, and left to right. An abrupt transition from a suspension of dispersed particles (at $I = 250$ mM) to an ordered, assembled array (at $I = I_t \approx 225$ mM) is observed. As I is reduced further, the clusters become amorphous and elongated, eventually ceasing to assemble.

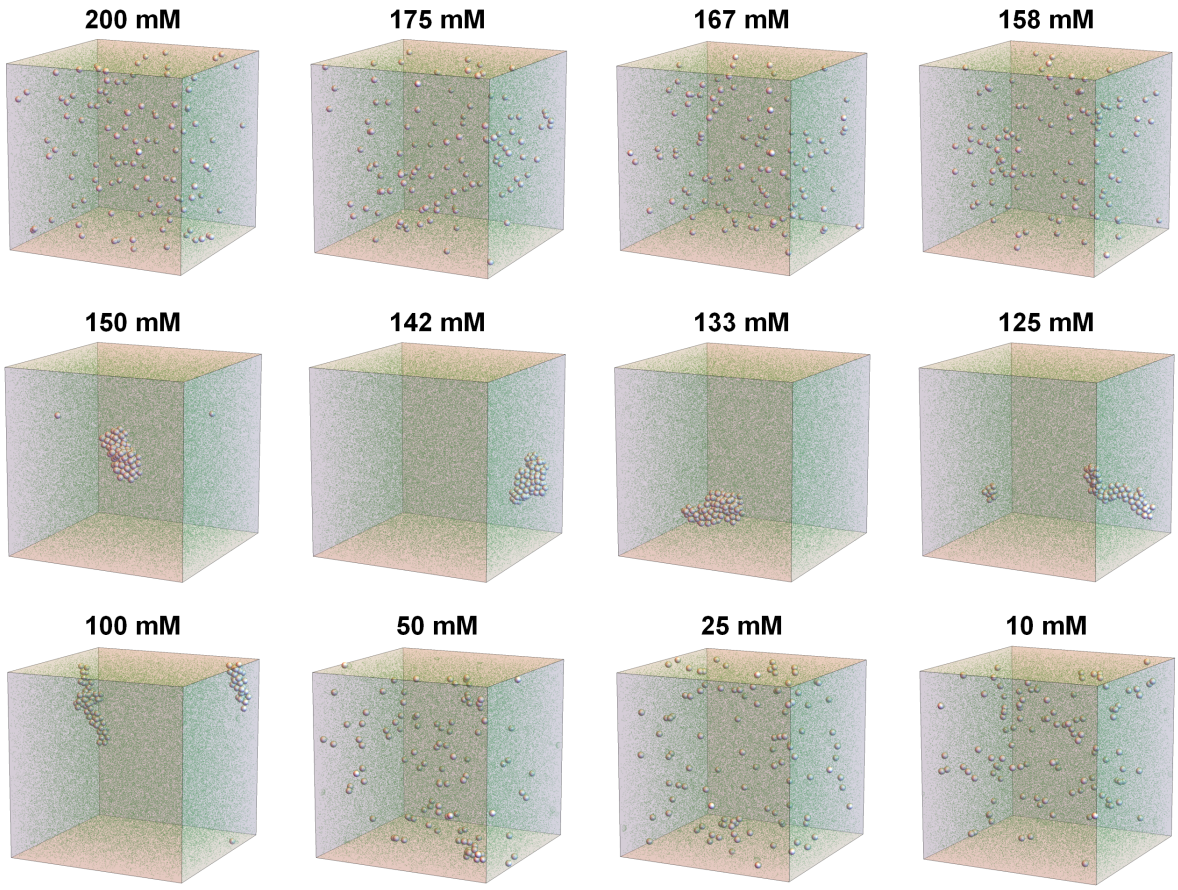

Figure S8: Representative snapshots of typical steady-state configurations of the P22-Q2 system; silver spheres are VLPs and smaller green spheres are dendrimers. Ionic strength I decreases from top to bottom, and left to right. An abrupt transition from a suspension of dispersed particles (at $I = 158$ mM) to an ordered, assembled array (at $I = I_t \approx 150$ mM) is observed. As I is reduced further, the clusters become amorphous and elongated, eventually ceasing to assemble.

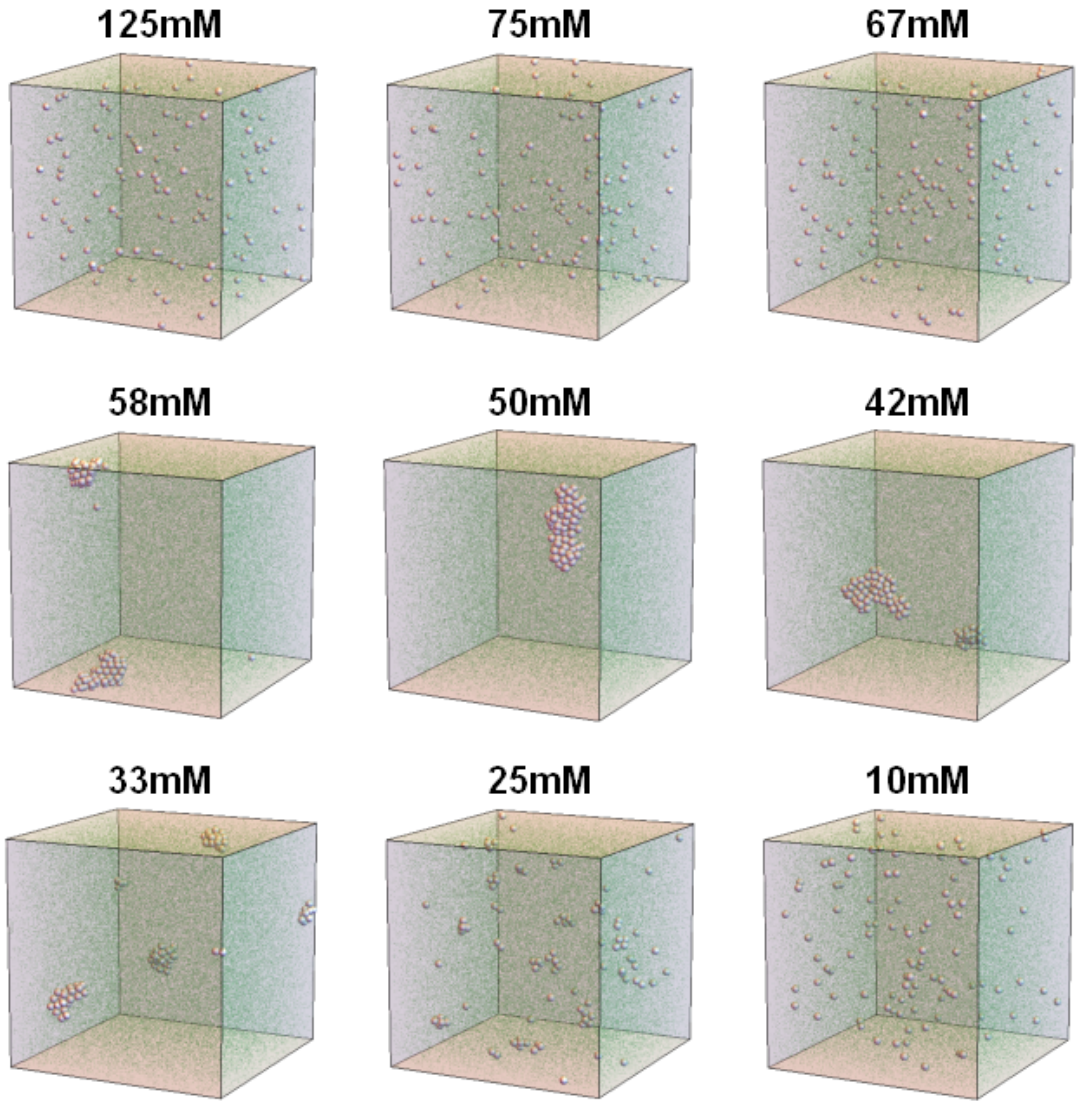

Figure S9: Representative snapshots of typical steady-state configurations of the P22-K2 system; silver spheres are VLPs and smaller green spheres are dendrimers. Ionic strength I decreases from top to bottom, and left to right. An abrupt transition from a suspension of dispersed particles (at $I = 67$ mM) to an ordered, assembled array (at $I = I_t \approx 58$ mM) is observed. As I is reduced further, the clusters become increasingly amorphous and disconnected, eventually ceasing to assemble.

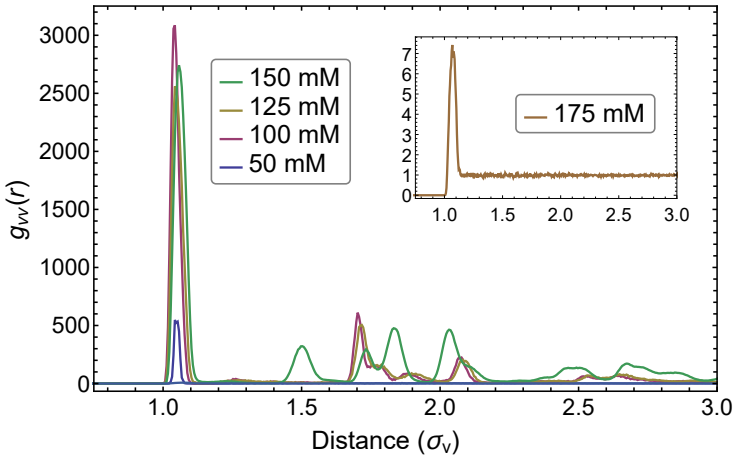

Figure S10: The VLP-VLP pair correlation functions for P22-Q2 system at different ionic strength I. Above the ionic strength threshold of $I_t \approx 150$ mM, the system is a weakly correlated solution of dispersed VLPs (inset); for $I \lesssim I_t$, an abrupt transition to an ordered array of VLPs is observed. Long-range order is diminished as I is reduced further.

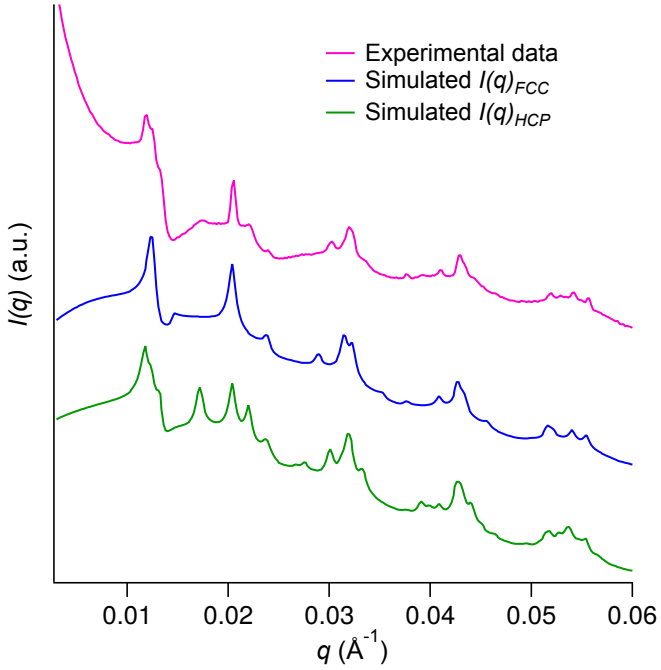

Figure S11: Comparison of experimental SAXS intensity $I(q)$ and theoretical plots of ideal FCC and HCP lattices. The lattice constant for FCC is 87.0 nm. HCP lattice constants are $a = 61.5$ nm and $c = 101.1$ nm. Data are scaled arbitrarily for visual clarity. This data shows the experimental results exhibiting features corresponding to both FCC and HCP lattices. This data is adapted from a previous publication.[3]

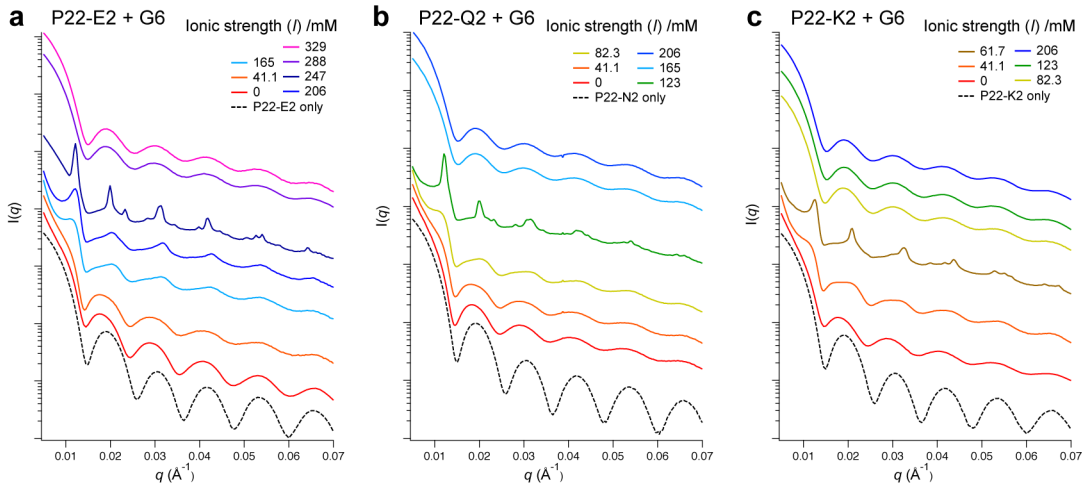

Figure S12: Measured SAXS patterns, $I(q)$ versus q, of (a) P22-E2, (b) P22-Q2, and (c) P22-K2 mixed with G6 dendrimer under various ionic strength conditions. Plots are vertically offset for clarity.

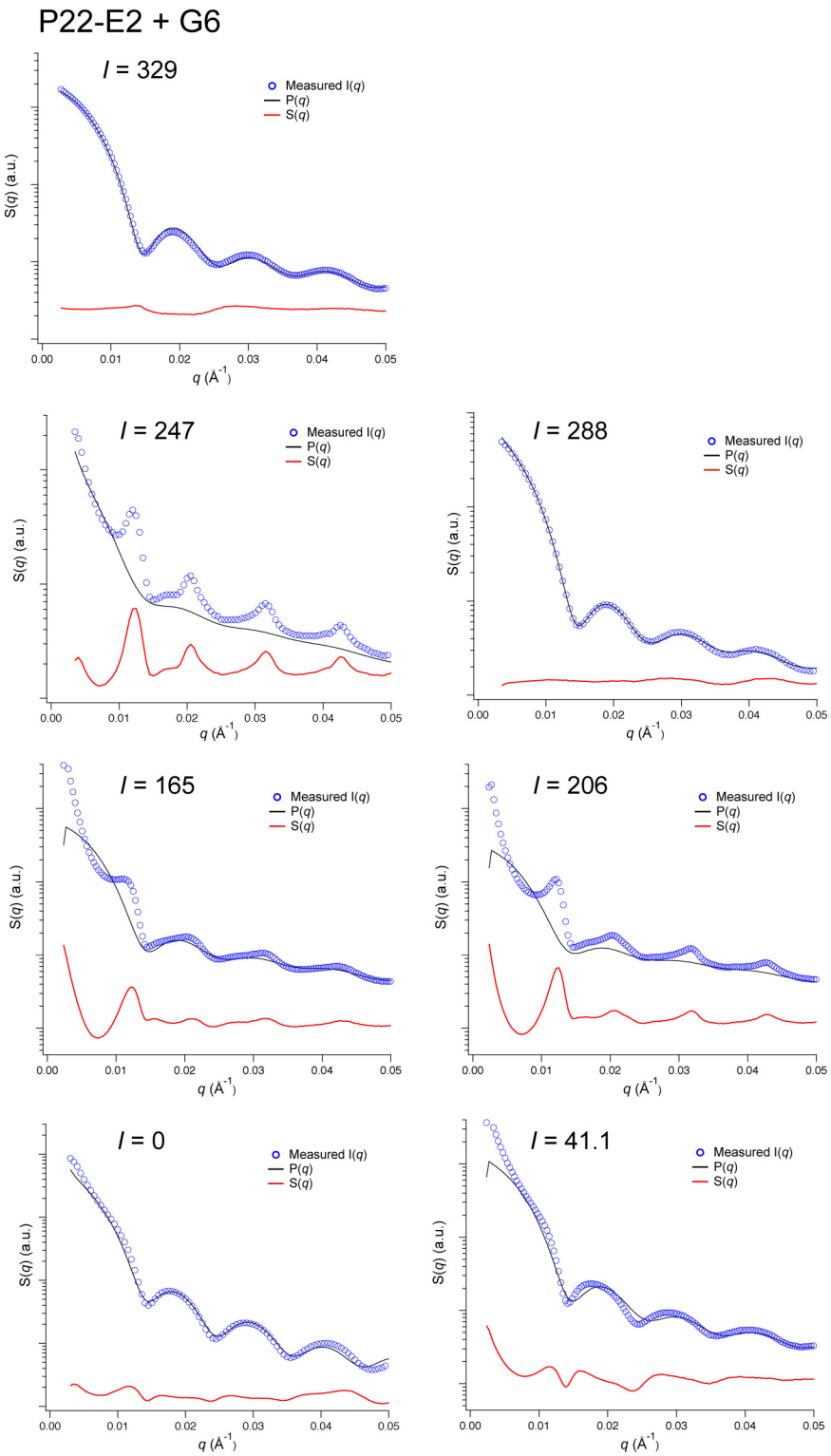

Figure S13: Plots of measured $I(q)$, modeled $P(q)$ and extracted $S(q)$ SAXS data. In all plots, the blue trace is the experimentally obtained $I(q)$ of each sample, and the black trace is the modeled form factor $P(q)$. The structure factor $S(q)$ (red trace) was obtained by dividing $I(q)$ by $P(q)$. The $S(q)$ plots are vertically offset for clarity.

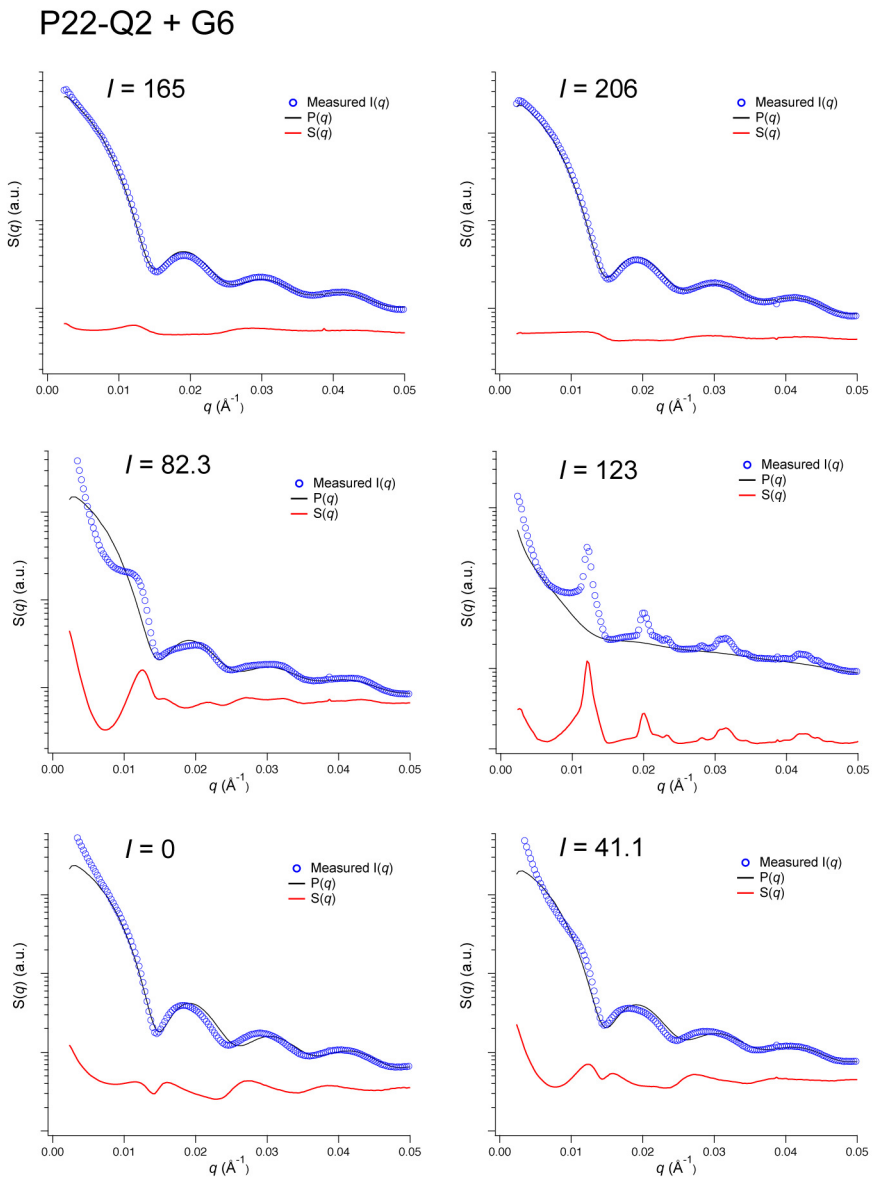

Figure S14: Continuation of Figure S13 for P22-Q2 assembly.

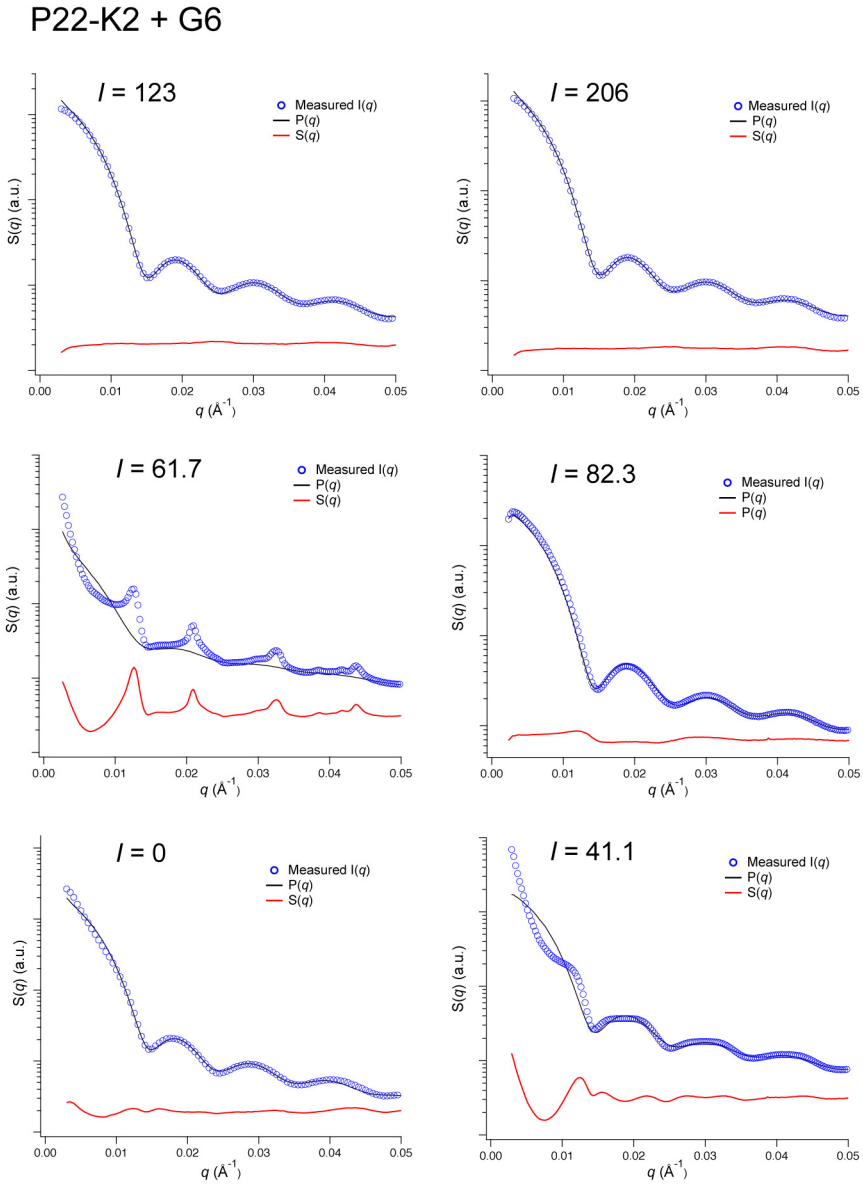

Figure S15: Continuation of Figure S13 for P22-K2 assembly.

P22-E2 + G6

I / mM	Δq_{samp} / Å	Estimated domain size / nm
0	0.00369	153.3
41.1	0.00329	171.8
165	0.00223	260.1
206	0.00175	337.8
247	0.00081	699.4
288	No Assembly	-
329	No Assembly	-

P22-Q2 + G6

I / mM	Δq_{samp} / Å	Estimated domain size / nm
0	0.00379	149.3
41.1	0.00339	167.0
82.3	0.00282	200.8
123	0.00100	564.6
165	No Assembly	-
206	No Assembly	-

P22-K2 + G6

I / mM	Δq_{samp} / Å	Estimated domain size / nm
0	0.00383	147.7
41.1	0.00298	189.7
61.7	0.00141	401.3
82.3	No Assembly	-
123	No Assembly	-
206	No Assembly	-

Figure S16: The full width at half maximum (FWHM) of the resolution-corrected, first-order diffraction peak and estimated domain size of arrays assembled from P22 variants and G6 dendrimers. The domain sizes of the assembled arrays increased with increasing ionic strength until the latter exceeded the threshold ionic strength for each P22 variant.

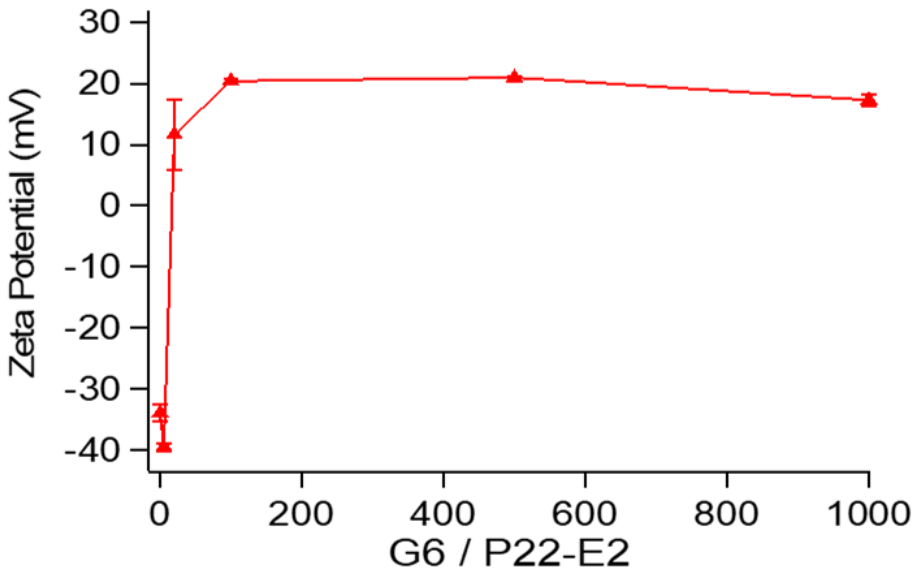

Figure S17: Zeta potential of P22-E2 arrays as a function of G6 dendrimer concentration c_d (measured as the number of dendrimers per P22-E2 VLP) at a low ionic strength of 10 mM ($n = 3$ measurements). The zeta potential of each P22-E2 without G6 was approximately -33 mV. When mixed with G6 dendrimer at $c_d = 5$, the zeta potential of the assembled array stayed negative at -39 mV. The zeta potential of the assembly shifted to a positive value (11 mV) when P22-E2 was mixed with G6 at a concentration of $c_d = 20$, and it reached to around 20 mV at $c_d = 100$. This charge inversion is likely due to over-condensation of G6 dendrimers on the VLP surface, in alignment with the predictions of the computational model.

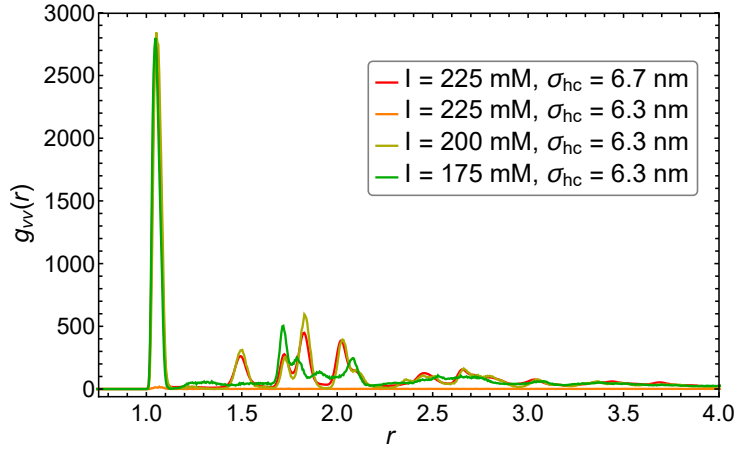

Figure S18: VLP-VLP pair correlation functions showing that increasing VLP-dendrimer steric repulsion (decreasing σ_{hc}) shifts the ionic strength threshold I_t downward. The P22-E2 ordered array (using $\sigma_{\text{hc}} = 6.7$ nm) with threshold $I_t = 225$ mM is shown for reference (red). The increased steric repulsion (for VLP systems with $\sigma_{\text{hc}} = 6.3$ nm) requires a stronger VLP-dendrimer electrostatic attraction to form the ordered array, lowering the ionic strength threshold downward to $I_t = 200$ mM. Further lowering of the ionic strength for the $\sigma_{\text{hc}} = 6.3$ nm system leads to a decrease in the long-range order.

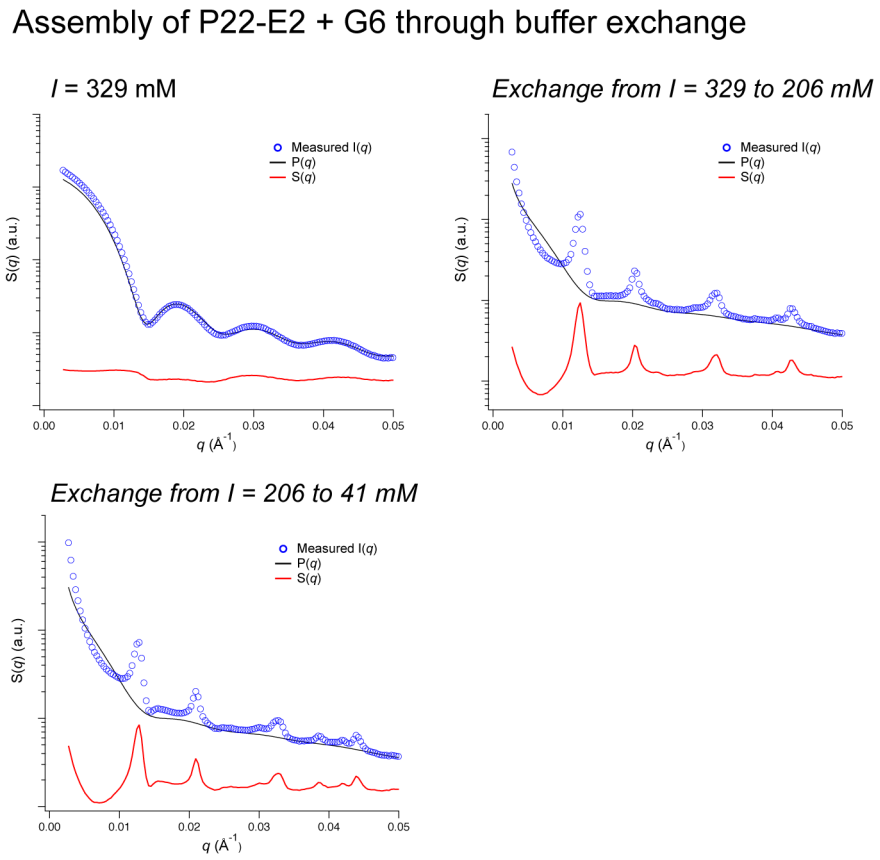

Figure S19: Continuation of Figure S13 during dialysis into lower salt conditions from above the ionic strength threshold I_t (top left), to at I_t (top right), and then at an ionic strength significantly below I_t (bottom).

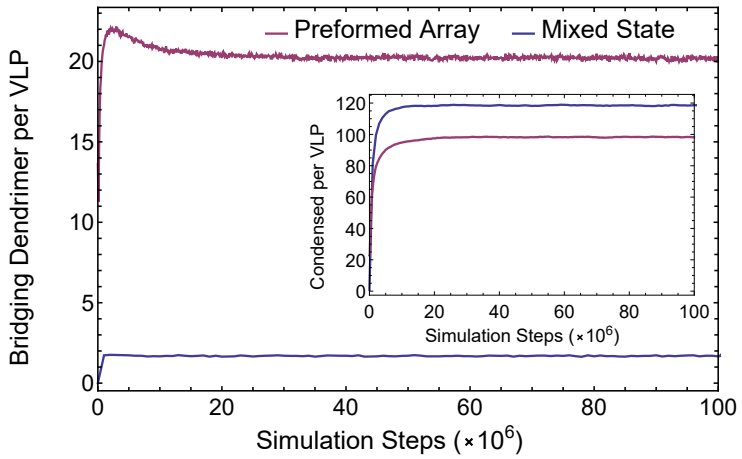

Figure S20: Simulated number of bridging dendrimers N_b per P22-E2 VLP at ionic strength $I = 50$ mM as a function of simulation steps (10^6 steps correspond to ≈ 1 microseconds). Blue curve shows the result for an initially randomly mixed state of VLPs and dendrimers at $I = 50$ mM. Purple curve shows the data for a system initially assembled into an ordered array at $I = I_t \approx 225$ mM and then dialysed to $I = 50$ mM. The ordered structure for the dialysed, preformed array (purple) persisted under low ionic strengths as N_b equilibrated around ≈ 20 (starting at $N_b(0) \approx 12$), but the randomly mixed state (blue) exhibited no ordered assembly due to the lack of bridging dendrimers ($N_b < 2$). Inset shows N_c, the corresponding number of condensed dendrimers per P22-E2 VLP for the two systems. The superlattice persisted despite exhibiting $N_c \sim 100$.

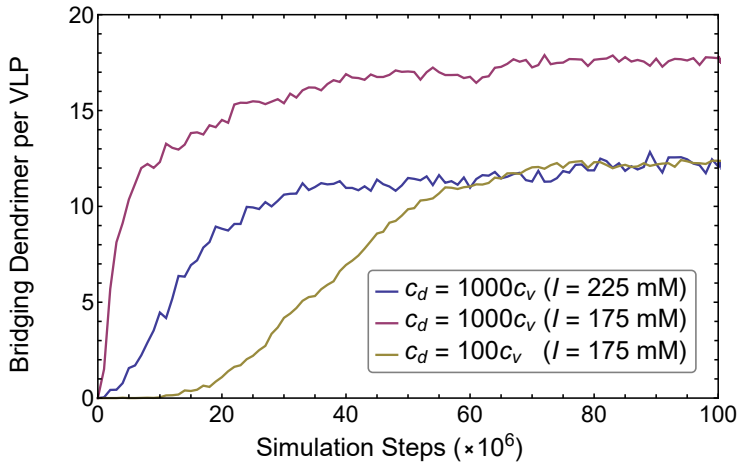

Figure S21: Number of bridging dendrimers N_b for the P22-E2 system where assembly into ordered structures was observed. Curves with different ionic strength I and dendrimer concentration c_d are shown. The curves at threshold (blue and gold) exhibit a similar lag phase with timescales of N_b saturation corresponding to the timescales of array formation. The curve not at threshold (purple) does not have a significant lag phase and corresponds to a system that becomes kinetically trapped in an amorphous state.

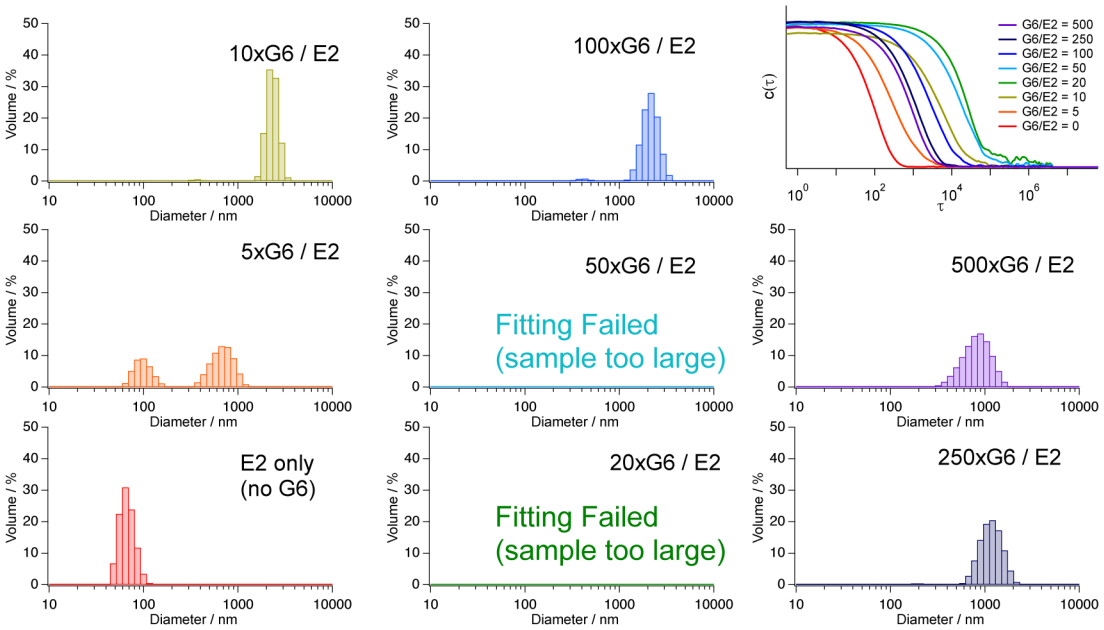

Figure S22: Correlation functions from dynamic light scattering measurements (top right), and corresponding volume-averaged hydrodynamic diameter distributions of P22-E2 VLPs mixed with G6 dendrimers at various concentrations c_d from 0 to 500 dendrimers per VLP in ionic strength of 10 mM (sodium phosphate 2.5 mM, sodium chloride 5 mM, pH 7.0). The size of the assembly increased with increasing c_d up to 50. At $c_d = 20$ and $c_d = 50$, fitting of the measured correlation function to obtain hydrodynamic size failed because the samples were too large. When c_d is increased further, the average size of the assembled arrays decreased to about 1 micrometers at $c_d = 500$.